MINE HEALTH AND SAFETY COUNCIL

Final Draft Report

TITLE

Spatial variation of seismicity in the Central Basin 2011

ENABLING OUTPUT 6

in project

Fluid-Induced Seismicity in the Central Basin Area: Ground Motion Prediction and the Development of an Early Warning System for Risk Reduction

Artur Cichowicz, Denver Birch, Lizelle Labuschagne, Tebogo Pule and Ian Saunders

Research Agency : Council for Geoscience

Project number : SIM 11-02-01

Executive summary

After 3.5 years since pumping water stopped in the ERPM mine, the evolution of seismicity over time indicates that the Central Basin area is not yet in equilibrium. Because the Central Basin seismicity is located directly beneath the densely populated area of Johannesburg a full understanding of its mechanism is required.

Over the last two years an increase in seismicity has been observed in the Central Basin area. This could be associated with the process of water flowing into old mining voids and the rising water level inducing changes in the stress state of the rock mass in the area.

In early 2010, the National Seismic Network was extended and a cluster of 12 strong ground motion seismograph stations was installed in the Central Basin area. A catalogue of 573 events was created from the recorded seismicity in the area. The catalogue consists of the following source parameters: location, magnitude, seismic moment, radiated seismic energy, corner frequency, static stress drop and apparent stress drop. Locations of seismic events are successful at capturing the general patterns of recent seismicity in the Central Basin. Most events are located within the boundaries of old mines. There is no observed diffusion process of migrating seismicity from east to west over the two year period. From the start of 2010, seismicity has been observed across the entire area. On the other hand, the most seismically active area is the ERPM mine.

Seismicity patterns and characteristics of source parameters provide a way to access the mechanical response of crustal materials. Relations between source parameters such as seismic energy versus seismic moment, seismic moment versus corner frequency, static stress drop versus apparent stress drop and static stress drop versus seismic moment are presented. These relationships are used to provide an understanding of the physical phenomena that occur in the medium due to voids flooding. The ranges of source parameter variations are presented. Analysis of data shows that the static stress drop and apparent stress drops of earthquakes have a tendency to increase with magnitude and seismic moment. This observation has a strong implication for the ground motion prediction for the maximum expected magnitude. Therefore, the above tendency should be investigated additionally to build confidence in the estimation of source parameters that control the ground motion prediction equation.

Table of contents

List of tables

List of Figures

1 Introduction

A study of the spatial variation of seismicity is the main objective of this report. A seismic event is classified using the following parameters:

- location
- origin time
- magnitudes, M_L and M_w
- seismic moments M_{0SH}, M_{0SV}, and M_{0P}
- radiated seismic energy
- corner frequencies for P-wave and S-wave
- static stress drop
- apparent stress drop

The observed seismicity is analyzed to reveal spatial clustering of seismicity across the Central Basin area. All possible seismicity patterns are being looked for: temporal clustering followed by long periods of quiescence and migration of seismicity from one area to another. The study region is divided into cells according to the level of seismicity.

The spatial variation of the following parameters is presented:

- number of earthquakes,
- cumulative radiated seismic energy
- the largest stress drops associated with seismic events
- the largest apparent stress drops

The observed seismic activity is used to establish relationships between the seismicity pattern, the mining void and geological features.

2 Seismic Source Parameters

The estimation of source parameters allows for the analysis of source parameters triggered by a rising water level in the Central Basin. Enabling output 2 presents the details of the method used to process waveforms. The path parameters are:

$$Path(f,r) = \begin{matrix} 1/r & \exp() & for & S-wave \\ 1/r & \exp() & for & P-wave \end{matrix} \quad (1)$$

A frequency dependent function that compensates for the near surface geology site effect is unknown at this stage. Only the κ_0 parameter, which controls the high frequency attenuation caused by near surface geology, is assumed. Kappa is set to a fixed value of 0.005 for all stations. The assumed attenuation parameters with an estimated seismic moment and corner frequency match the observed spectra well.

2.1 M_w and M_L Magnitudes

Magnitude M_w obtained from the Hanks & Kanamori (1979) relationship is most often used as it relates to seismic moment in a stable and objective way:

$$M_w = 2/3\,(\log_{10} M_0 - 9.1) \quad (1)$$

where M_0 is seismic moment.

The relationship between M_w and M_L magnitudes is presented on Figure 1 and numerical values are given by equation 2 with a correlation coefficient between magnitudes of 0.73. This relation is very important to compare data from mining networks with data from the CGS network. M_L magnitude is usually used by national networks around the word.

$$M_w = 0.47\,M_L + 0.95 \quad (2)$$

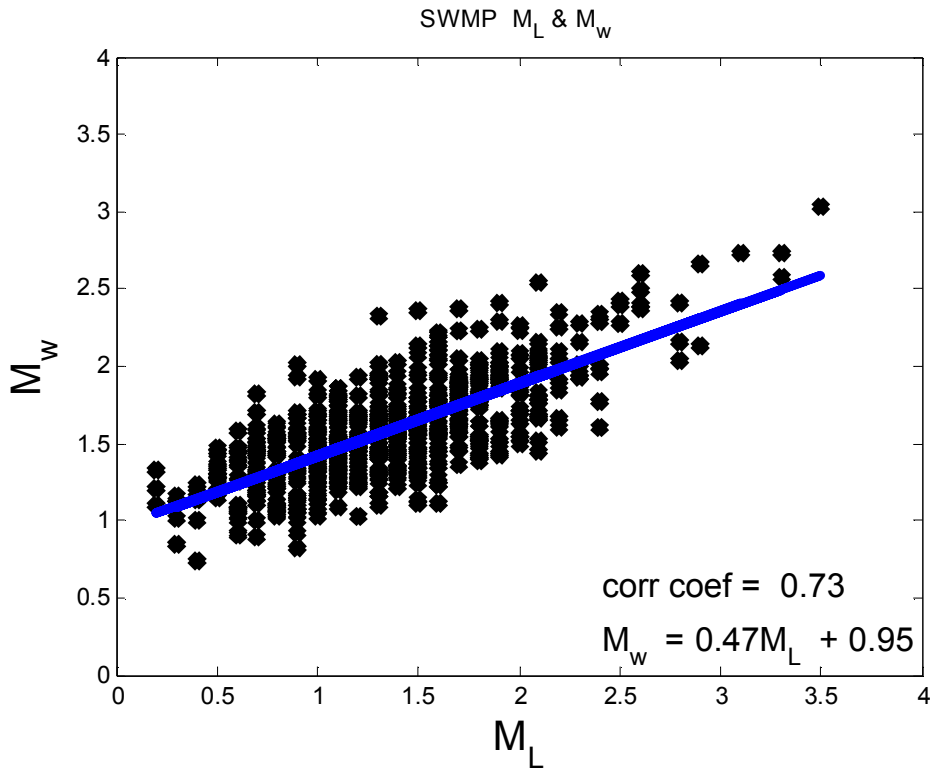

Figure 1. Relationship between magnitudes M_L and M_w.

2.2 Relationships between Seismic Moments and Radiated Seismic Energy.

Several tests were performed to verify the estimated parameters. Figure 2 shows relationships between seismic moments M_{0SH} versus M_{0SV} and M_{0P} versus M_{0SV}. The correlation coefficients between the seismic moments are 0.99 and 0.94. Those high values indicate that the three series of independent measurements of the M_{0SH}, M_{0SV}, and M_{0P} are accurate.

An average M_{0SH} seismic moment is 2.5 times bigger than an M_{0SV}. In the environment, where near surface geological structure amplifies vibration in the SH direction, it is expected, that the M_{0SH} seismic moment should be higher than the M_{0SV} seismic moment. At this stage of the project the site effect has not yet been removed. The M_{0P} seismic moment is 4.5 times larger than the M_{0SV} seismic moment. The P-wave seismic moment was obtained using an average value from the three components of ground motion. In a perfect homogeneous medium the S-wave and the P-wave seismic moments should be equal. The observed difference could suggest systematic differences in correction factors such as geometrical spreading, path attenuation or site effect. When the effect of the above factors is estimated and differences still exist, it could be attributed to a particular seismic source mechanism in the Central Basin.

The seismic energy radiated by the rupture process and the seismic moment are two of the most fundamental earthquake-source parameters. The seismic moment and radiated energy relation is the most important characterization for a group of events. Figure 3 shows the relationship between the E_{0SV} seismic energy and the M_{0SV} seismic moment. The earthquakes in the database span a range of seismic moments of roughly 3.5 orders of magnitude from 10^{10} to $5x10^{13}$ Nm. For the same earthquakes, the seismic energy range is from 10^2 to 10^9 J.

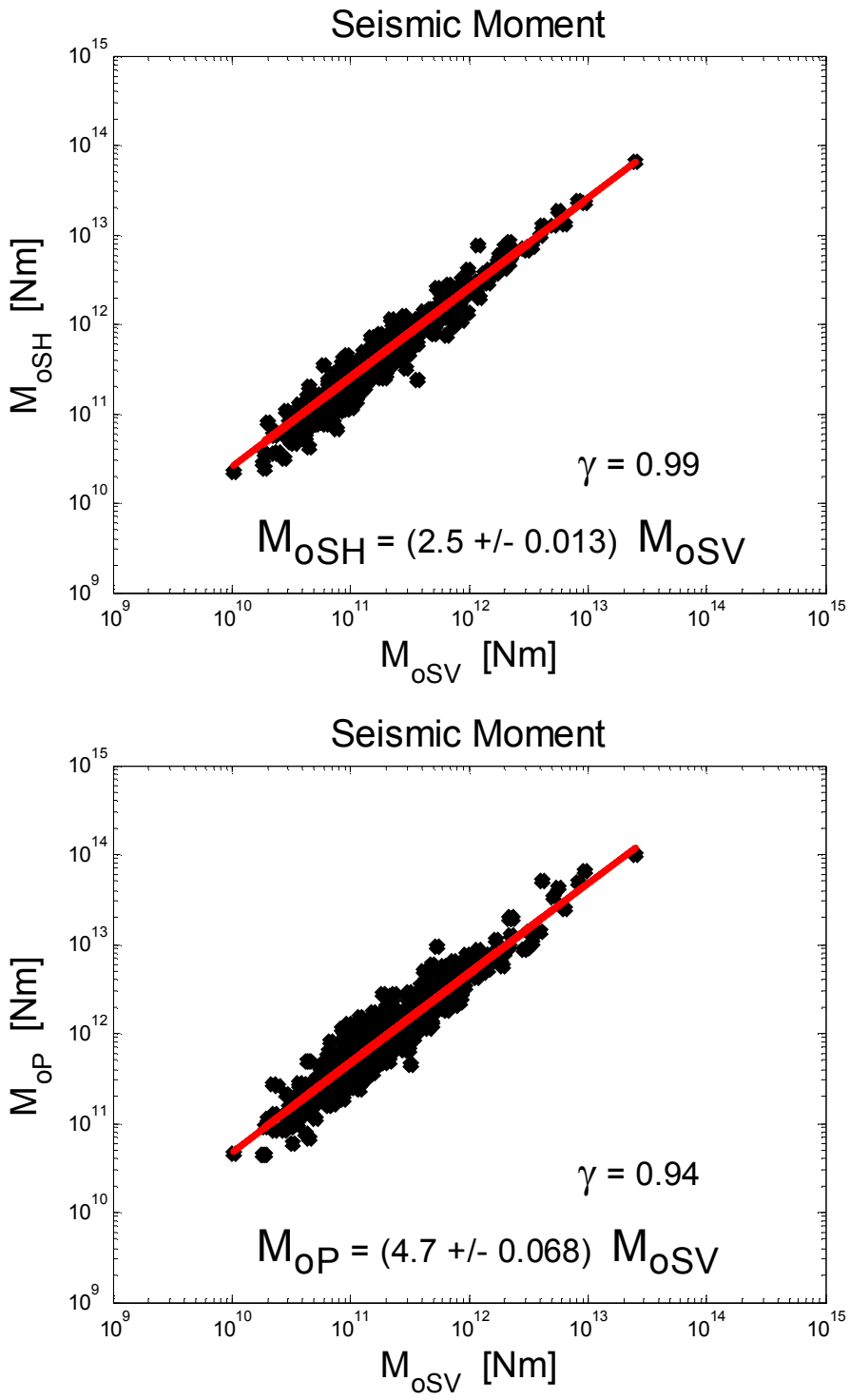

Figure 2. Relationship between seismic moments: M_{0SH} versus M_{0SV} and M_{0P} versus M_{0SV}. .

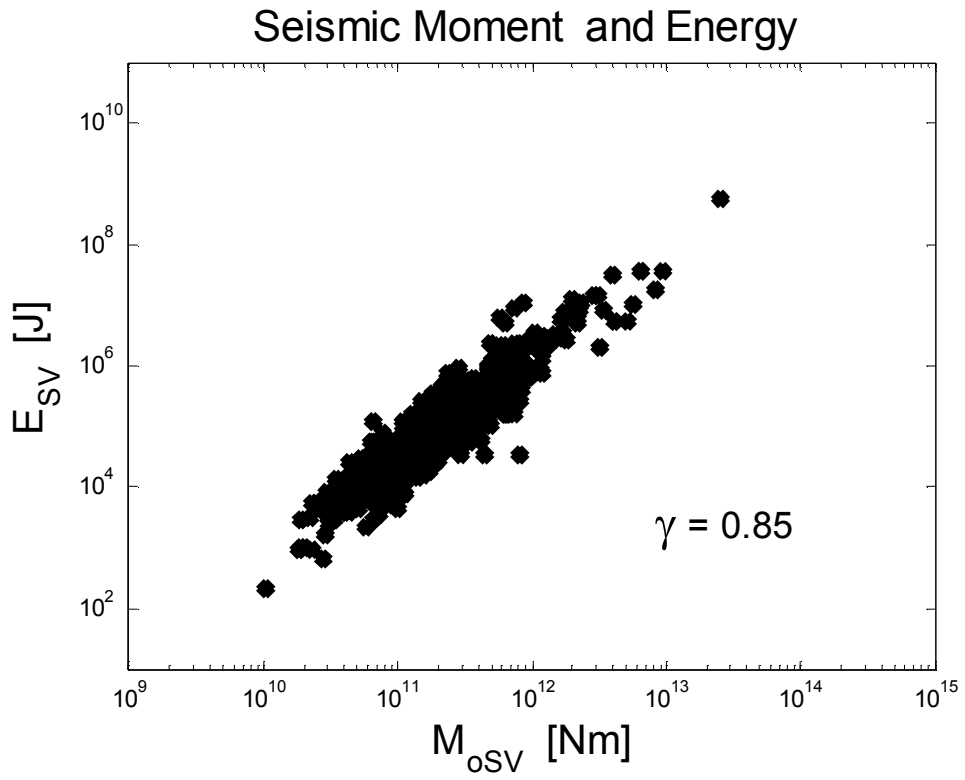

Figure 3. Relationship between seismic moment and radiated seismic energy for SV component.

The ratio of radiated energy to seismic moment, multiplied by the shear modulus yields the apparent stress:

$$\Delta\sigma_{app} = \mu\frac{E_0}{M_o} \quad (2)$$

The apparent stress drop is different from the stress loading the fault. The apparent stress drop is the stress that causes seismic energy radiation. For the earthquakes analyzed in this study, the apparent stress drop calculated from the S waves varies between $2x10^{-3}$ to 3 MPa.

Figure 4 shows the relationship between $\Delta\sigma_{app}$ and M_0. This figure clearly displays that the larger apparent stress drop is associated with a larger

seismic moment. This observation has strong implications for the seismic hazard estimation as it contributes to understanding the scaling relationship.

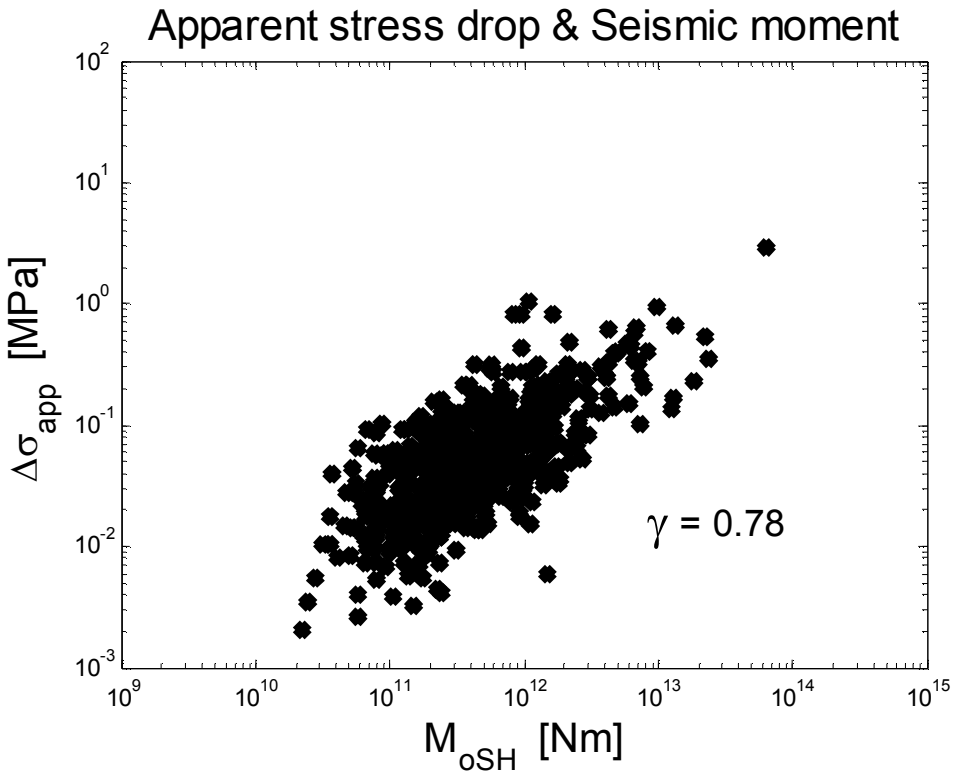

Figure 4. Relationship between apparent static stress drop and seismic moment

Seismic moment, seismic energy and apparent stress drop are useful, not only because they all have well-defined physical significance, but also because their estimates entail no model dependence. They measure different aspects of the earthquake source that permit one to relate earthquakes to various factors, such as crustal deformation, damaging ground motion and lithospheric strength (McGarr and Fletcher, 2002)

2.3 Estimation of Corner Frequencies and Static Stress Drop

The corner frequency measurement is a very important parameter used for the estimation of source size and static stress drop. Figure 5 shows the relationships between $f_{0P,}$ f_{0SV} and f_{0SH}. These relationships have values close to 1. It is expected that for shear fracture processes, a corner frequency of the P-wave should be larger than the S-wave. The corner frequencies vary from 6 Hz to 45 Hz. Once the values of attenuation for the Central Basin are known, the relationship between corner frequencies will be recalculated.

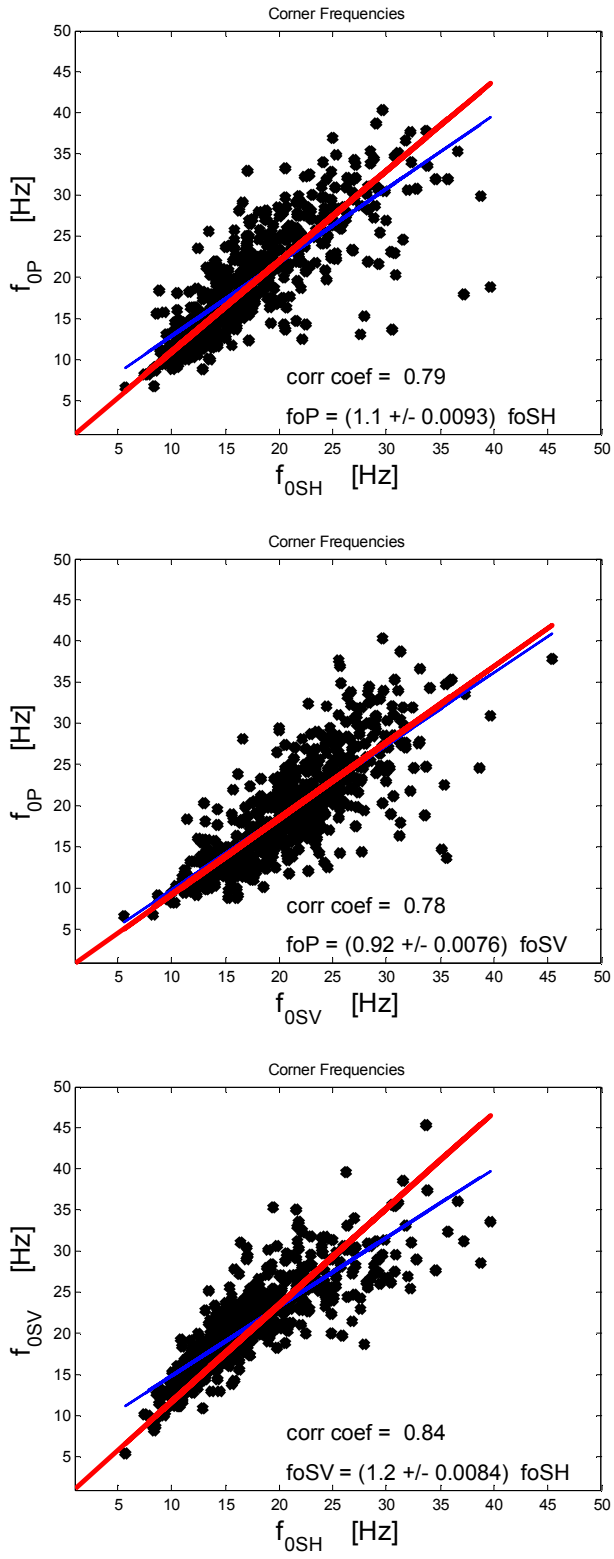

Figure 5. Relationship between corner frequencies: (red) the least squared solution, (blue) polynomial fit in a least squares sense.

Static stress drop is estimated using the seismic moment and corner frequencies measurement obtained from the P- and S-waves. The relationship between static stress drops and apparent stresses of analyzed events is shown in Figure 6. It clearly shows that both static stress drops and apparent stresses are estimated with a high correlation coefficient.

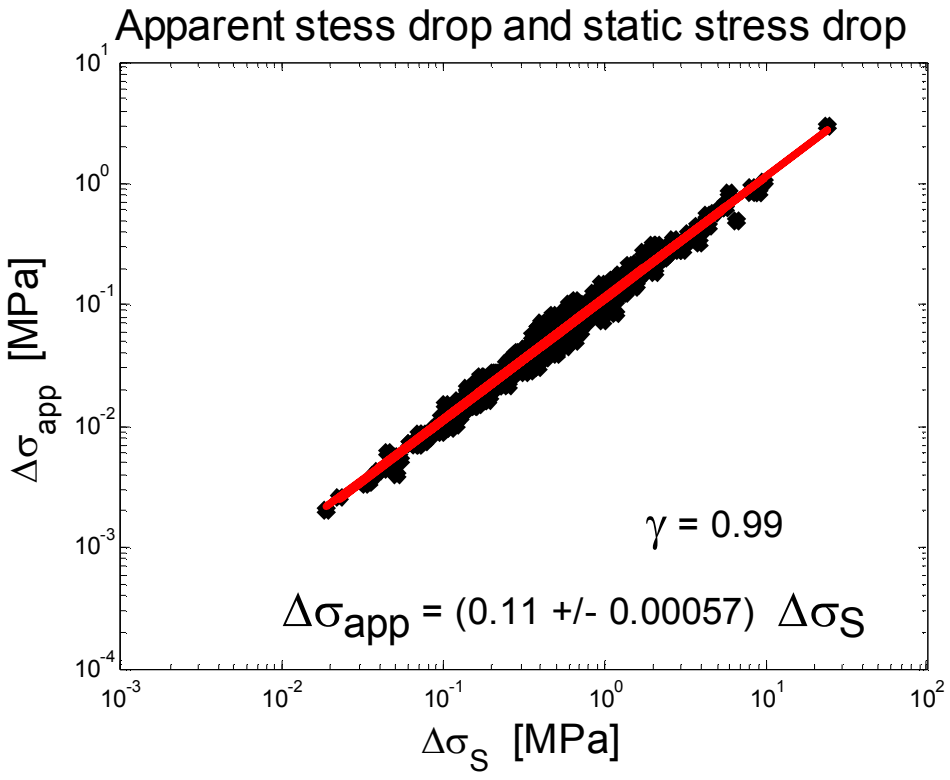

Figure 6. Relationship between apparent static stress drops and static stress drops obtained from waveforms of the S-wave.

Relations between seismic moments and corner frequencies are one of the most important characteristics of seismic parameters for the studied area. Figure 7 shows seismic moment versus corner frequencies for the S-waves and P-waves. Diagonal lines show constant stress drops. Most of the seismic events have static stress drops in the range of 0.1 MPa to 5 MPa.

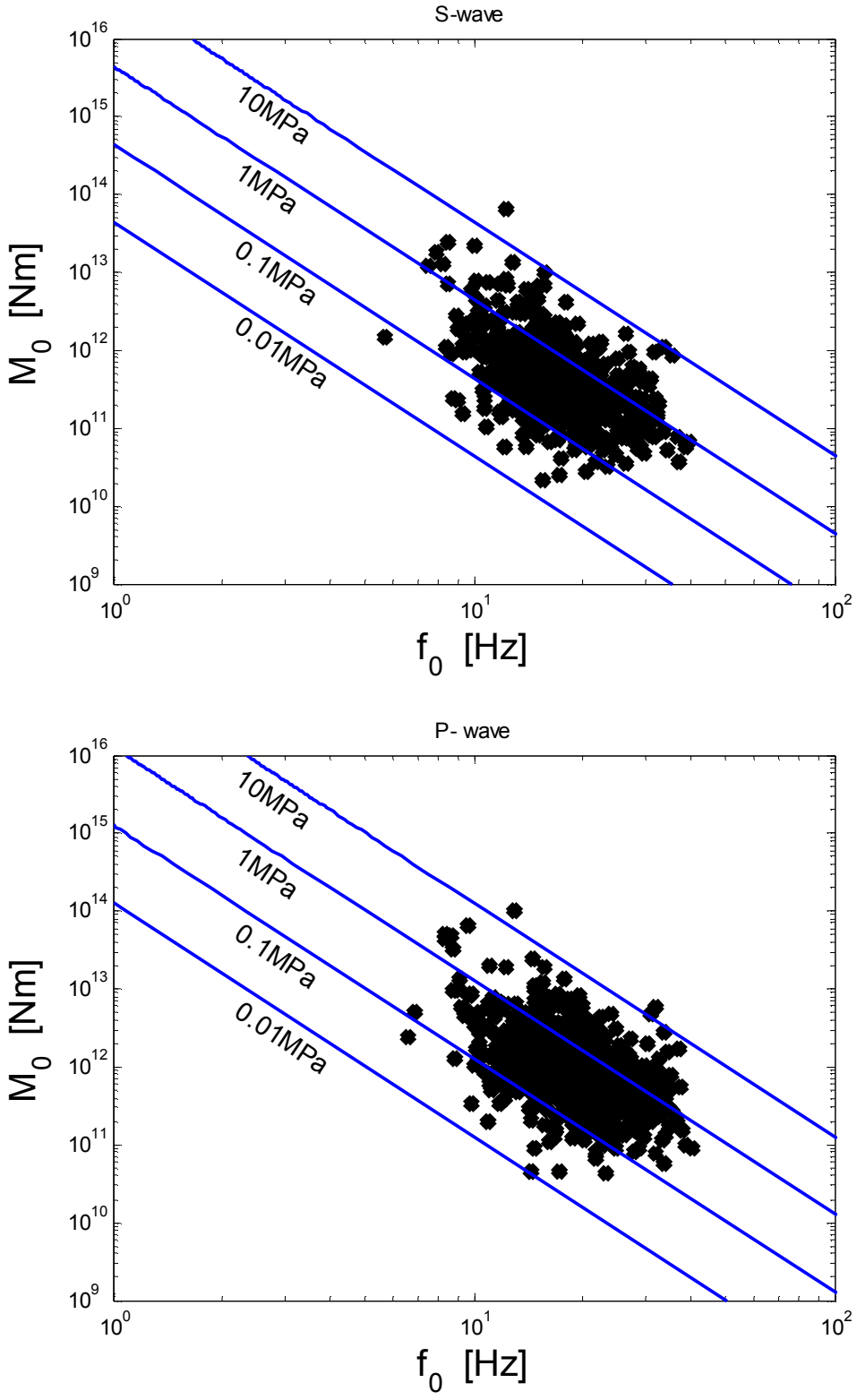

Figure 7. Seismic moment versus corner frequency for the P- and S- wave. Blue lines follow constant static stress drop.

2.4 Relationship between Stress Drop and Seismic Moment

The static stress drops obtained from the S-wave and P-wave should have similar values. In order to verify the quality of results of the seismic source estimations, Figure 8 shows the static stress drop obtained from both types of body waves. The correlation coefficient is relatively large and has a value of 0.88. The relationship between both estimations is close to 1. Because the stress drop is very sensitive to small errors in the estimation of corner frequency, the result presented in Figure 8 suggests that the processing of spectral parameters is very consistent.

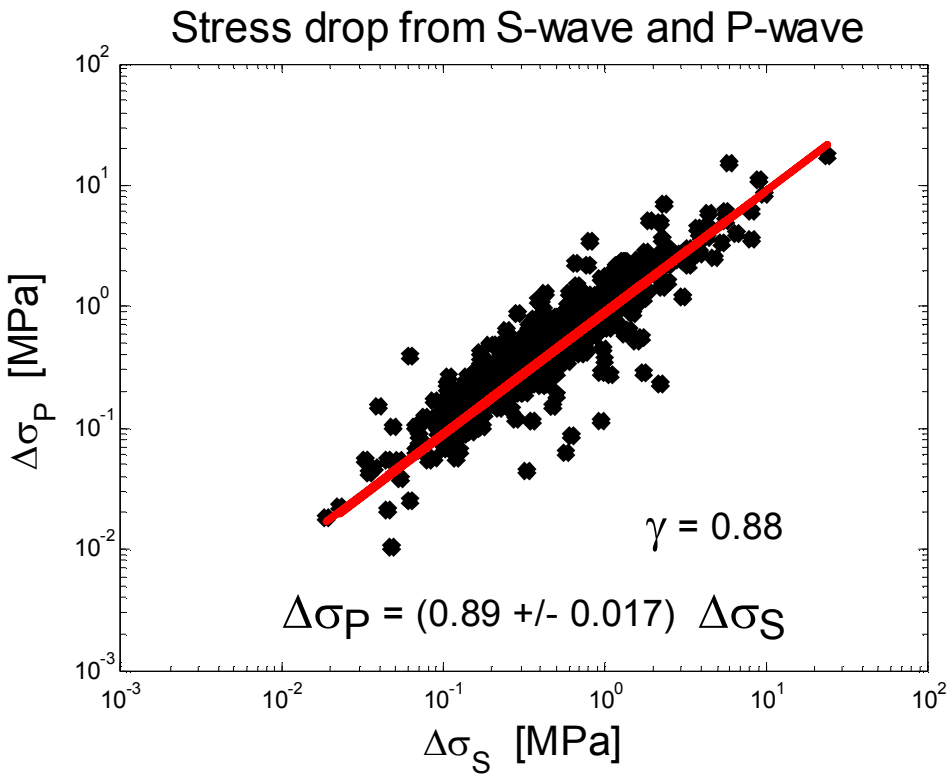

Figure 8. Relationship between static stress drops obtained from waveforms of the P- and S-wave.

The seismic hazard assessment relies very heavily on the assumed static stress drop for the largest expected magnitude. Therefore, understanding the relationship between seismic moment and stress drop is of great importance. Figure 9 shows the above relationship for the Central Basin region. The researchers preparing US national seismic hazard maps assume a change in the scaling law between small and large earthquakes (>5), with stress drops increasing for the largest earthquakes. The observed relationship contributes to the scaling law for small low magnitudes (see Figure 9).

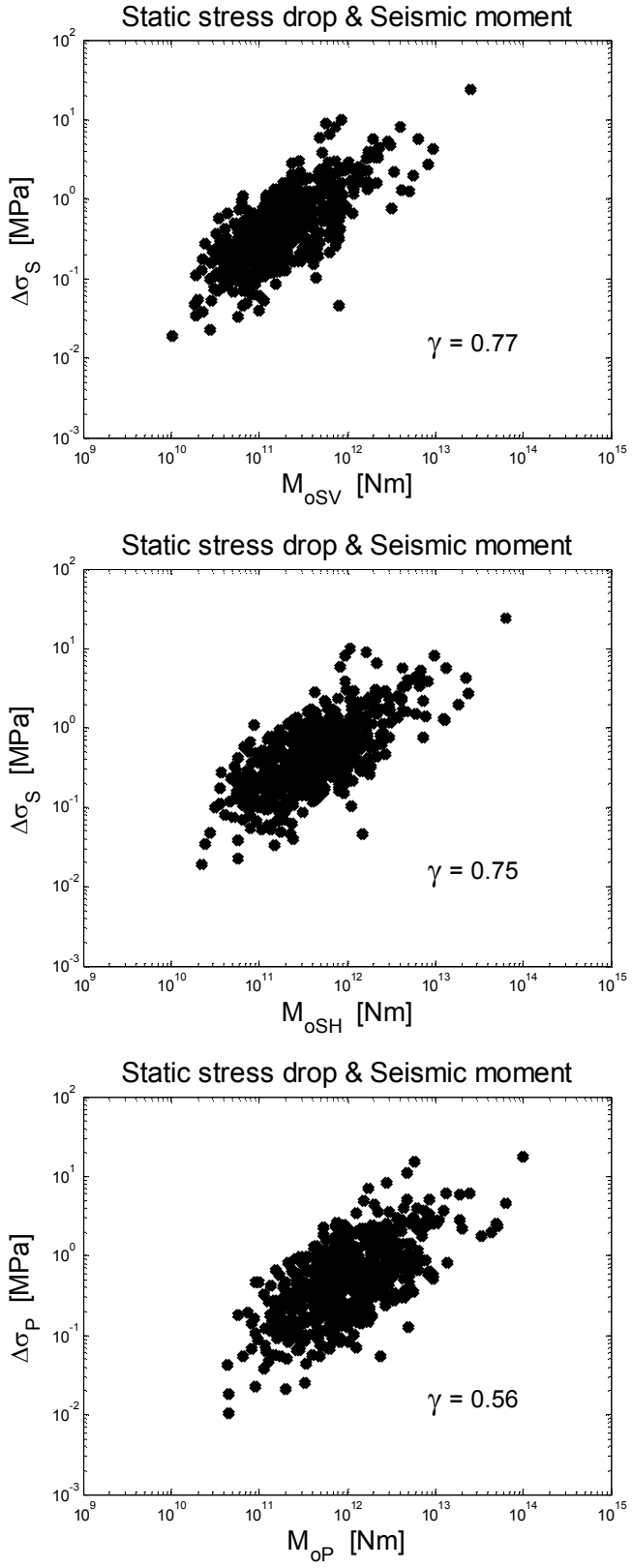

Figure 9. Relationships between static stress drop and seismic moment

3 Spatial and Time Variation of Seismicity in the Central Basin Area.

A catalog of earthquakes suitable for the estimation of spectral parameters contains 573 events that occurred between March 2010 and November 2011. Information about the distribution of seismic events in the Central Basin is presented in different ways. Figure 10 and 11 show distribution of seismicity in the Central Basin. Figure 11 (top) displays sizes of dots proportional to magnitudes. Figure 11 (bottom) provides a 3D view of seismicity. The lengths of blue vertical lines are proportional to magnitudes. The seismicity pattern shows that the largest events are located south of the Central Basin region (area of ERPM mine).

The distribution of earthquake magnitude in a region can be described by a frequency magnitude distribution and cumulative frequency magnitude distribution. In seismology the cumulative frequency magnitude is known as the Gutenberg-Richter relationship, $\log N = a - bM$, where N is the cumulative number of earthquakes with magnitudes larger than or equal to M, and '*a'* and '*b'* are constant. That describes the overall activity of a region and the relative distribution of earthquakes by magnitude, respectively. The parameter '*b'* is estimated as the slope of the best-fitting line for a prescribed magnitude range (Aki, 1965). Frequency-magnitude relationships for the Central Basin regions are plotted in Figure 12. The top graphs show events grouped with the same magnitude value per bin. The bottom graphs show the same data but magnitude values are grouped into 10 bins. The top graphs are suitable for calculating the 'b' value and the bottom graphs are used for visual inspection to evaluate the seismicity in the area.

From Figure 12 one learns that magnitudes near zero are sometimes reported, but that the maximum number of observations is for magnitude 1.1,

suggesting that the magnitude of completeness is generally larger than 1.1, but it may also be near 1.5 in some locations. The completeness of magnitude is defined as the magnitude at 0.85 of the maximum level of the cumulative frequency distribution or as the magnitude at 85% of the Gutenberg-Richter power-law fit of the cumulative frequency distribution.

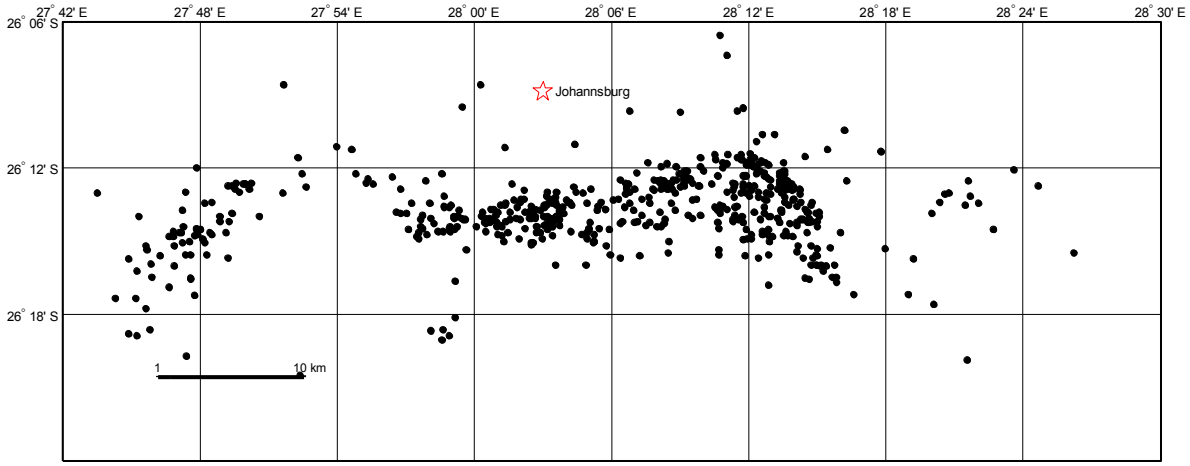

Figure 10. A map view showing epicenter locations for earthquakes in the Central Basin: black dots represent location of the seismic events.

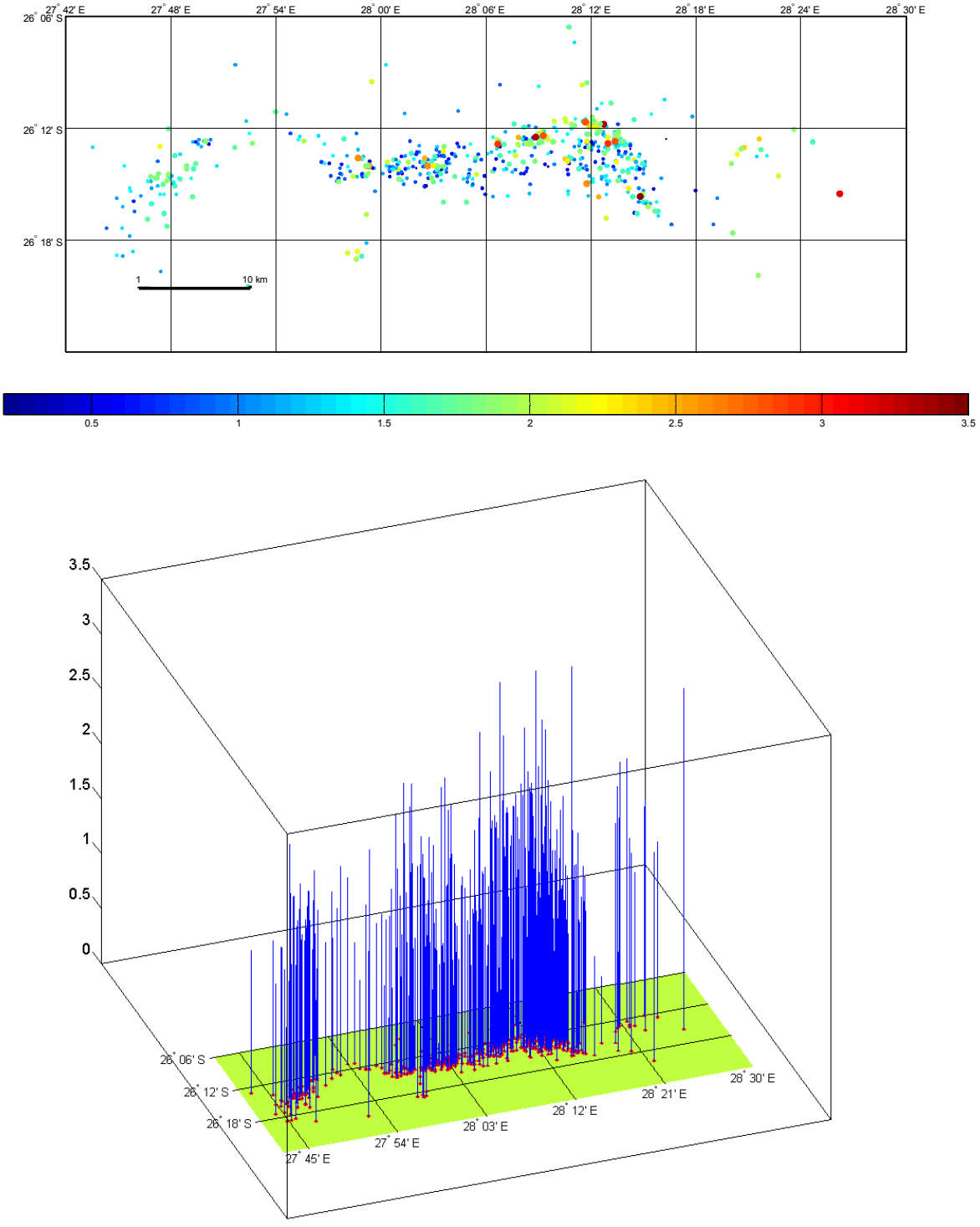

Figure 11. A map view showing epicenter locations of earthquakes in the Central Basin. (top) Sizes and color of dots represent different magnitudes of the seismic events. (bottom) A 3D map view showing epicenter locations where the lengths of blue lines are proportional to magnitude.

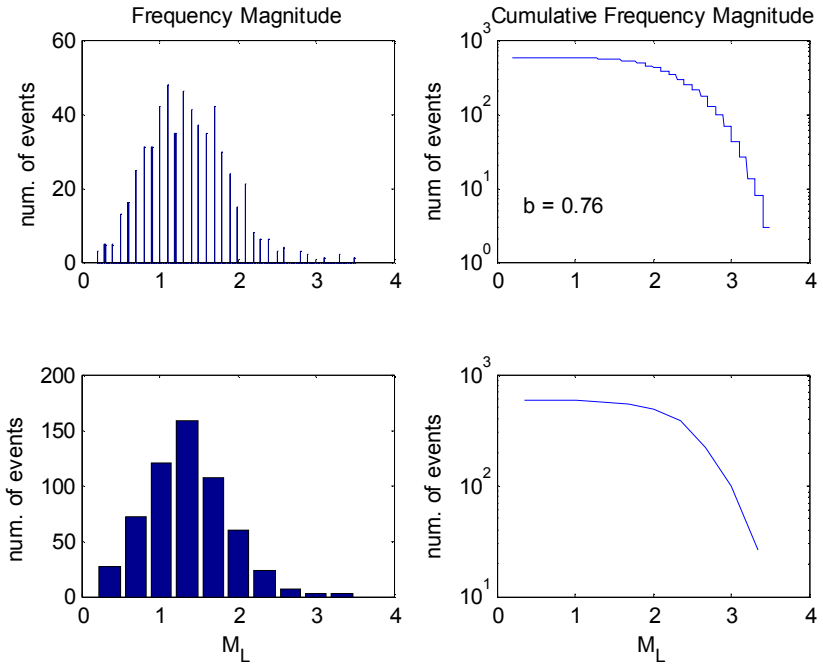

Figure 12. (left) Histograms of frequency magnitudes for all data from the Central Basin. (right) Cumulative frequency magnitudes.

3.1 Spatial Variation of Seismic Parameters

The spatial patterns of seismic energy radiated by earthquakes are shown in Figure 13. This figure shows a distribution of seismic events, where the size of dots is proportional to radiated energy in linear scale (top) and in log scale (bottom). From this map one can gauge the amount of energy radiated by the biggest earthquake of magnitude 3.5 (see Figure 13, top). The spatial pattern of seismic energy in log scale is shown as well (see Figure 13, bottom). The log scale reveals that the distribution of events with energy 10^{7}-10^{8} [J] has been observed across the entire area of the Central Basin. The histogram of

earthquakes with radiated energy reveals that 250 events have energy of 10^5 J (see Figure 14).

The static stress drop is presented in map view and in 3D view. The spatial distribution of static stress drops obtained from the S-wave waveforms and the apparent stress drops are shown on Figure 16 and 17. The earthquakes with the largest stress drops are observed in the eastern part of the basin (ERPM mine area) and in the central part of the basin.

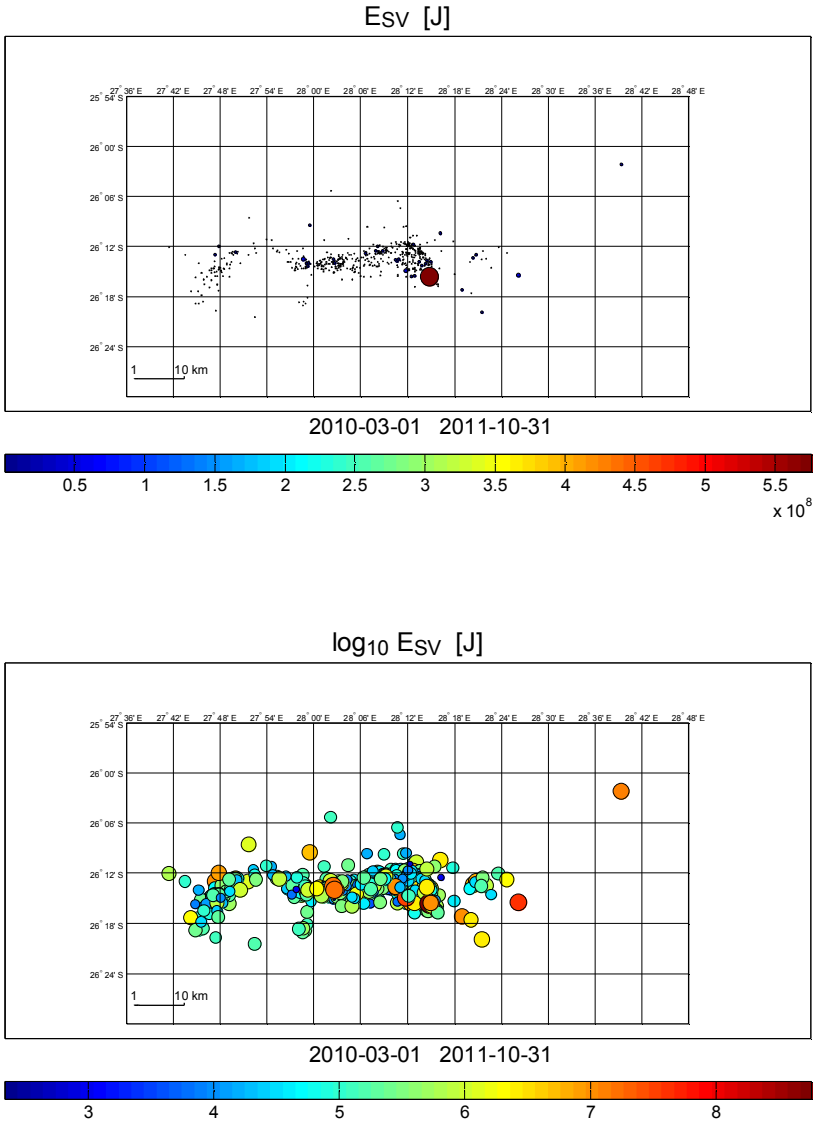

Figure 13. Distribution of seismic events where size of dots is proportional to radiated energy in linear scale (top) and in log scale (bottom).

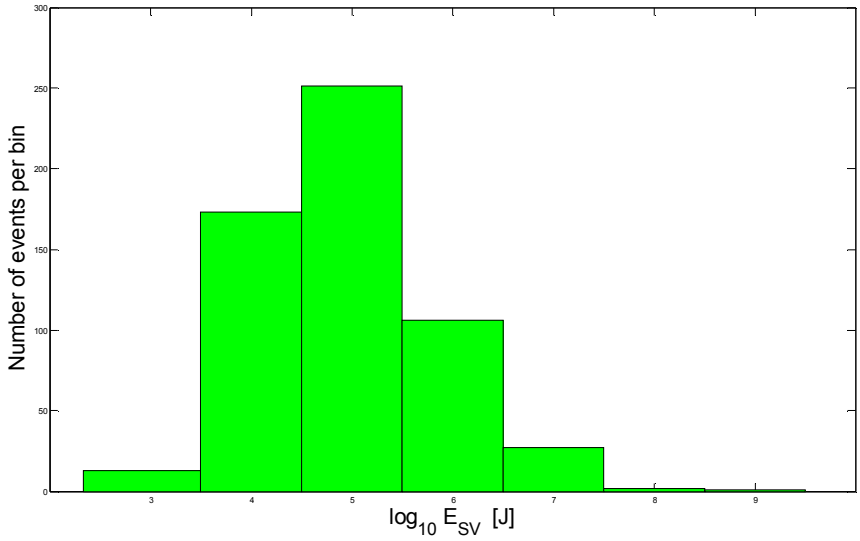

Figure 14. Histogram of log of seismic energy for the Central Basin area.

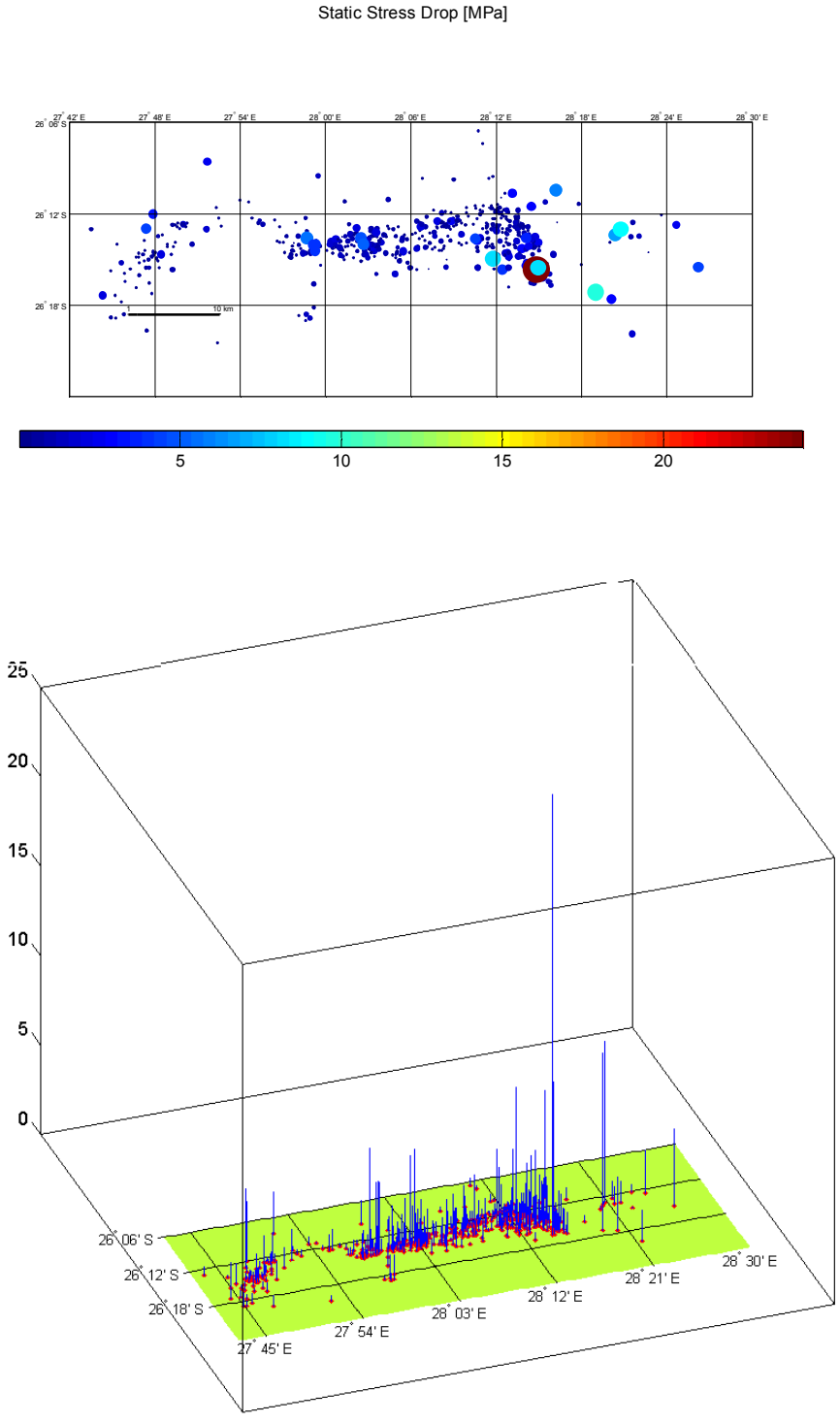

Figure 15. Distribution of seismic static stress drop events, where size of dots is proportional to the value of static stress drop in linear scale (top) and in log scale (bottom).

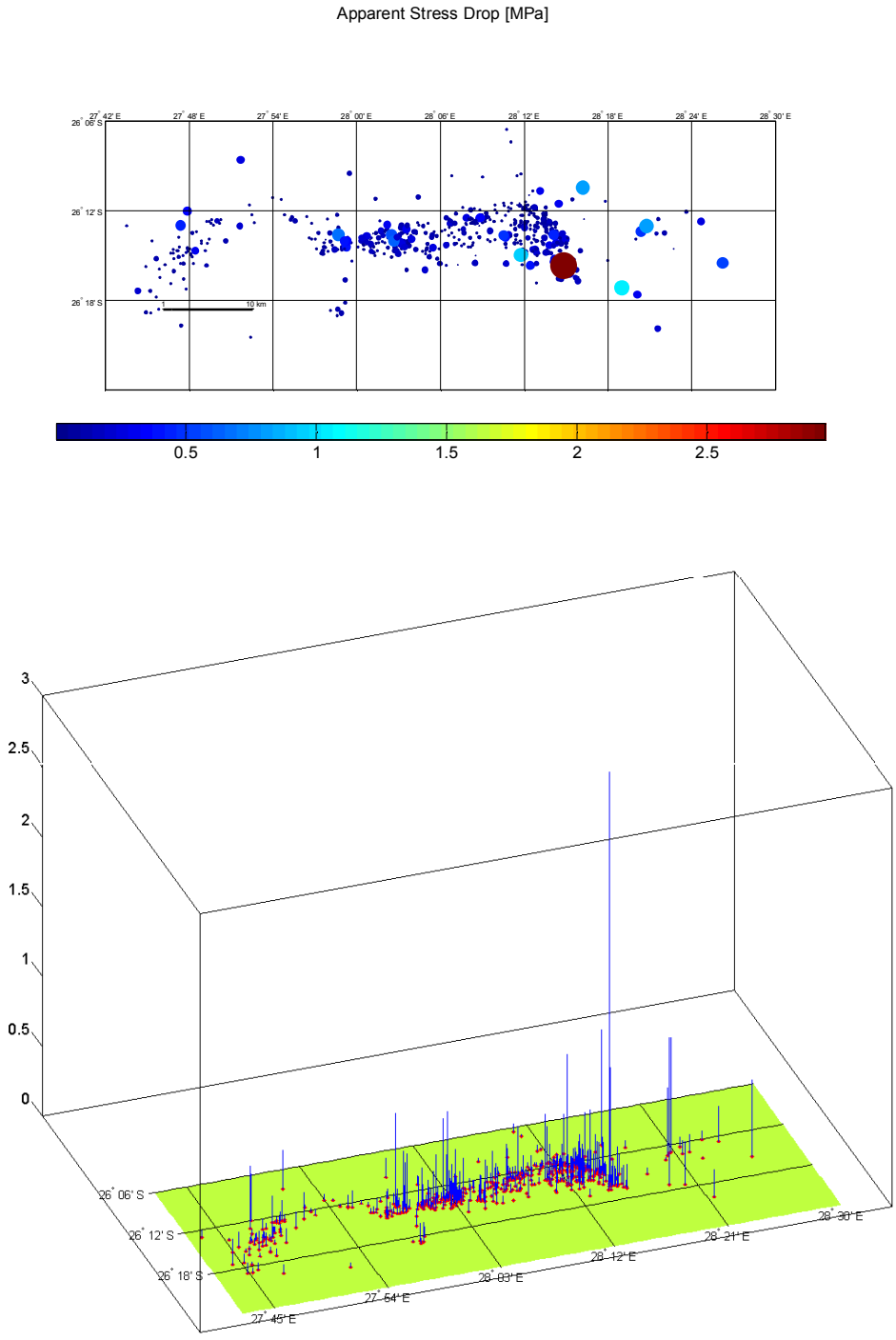

Figure 16. Distribution of seismic apparent stress drop events, where size of dots is proportional to the value of apparent stress drop in linear scale (top) and in log scale (bottom).

3.2 Identification Polygons with Dense Seismicity

The seismicity fluctuations in space are studied by dividing the Central Basin into polygons of equal area. The areas of polygons are selected arbitrarily. Table 1 shows three examples of polygons 10 km x 10km, 4 km x 4 km and 2 km x 2 km. Analyses include all polygons that have at least one earthquake per polygon (see Table 1 column 3, Figures 17, 19, 21, top). The number of earthquakes' occurrences in these polygons are shown on Figures 17, 19 and 21 (bottom). An attention-grabbing feature is that clusters located in the center and east part of the studied area have the most earthquakes per polygon. In general, the seismicity is concentrated in small clusters, while some scattered epicenters also exist.

In the next steps, the cumulative radiated energy per polygon is obtained. In the 3D view, Figures 18, 20 and 22 (top) show cumulative radiation energy per polygon. These graphs are dominated by the energy of the 3.5 magnitude earthquake. However, Figure 18 (top) shows that several other polygons have a significant contribution to radiated energy in the Central Basin. Figures 18, 20 and Figure 22 show histograms of cumulative radiated energy in log scale. The seismic energy radiated per polygon varied from 10^5 to 8 10^8 J (see Figure 18 and 20, bottom). This spans about 4 orders of magnitude from polygon to polygon, which is significantly smaller than the variation of seismic energy from the smallest to the largest earthquake (7 orders).

Table 1. List of polygons used to model the seismicity patterns

Nr	Polygon Area	Number of polygons	Figures
1	10 km x10 km =100 km ^{2}	25	17 and 18
2	4 km x 4 km = 16 km ^{2}	64	19 and 20
3	2 km x 2 km = 4 km ^{2}	125	21 and 22

;

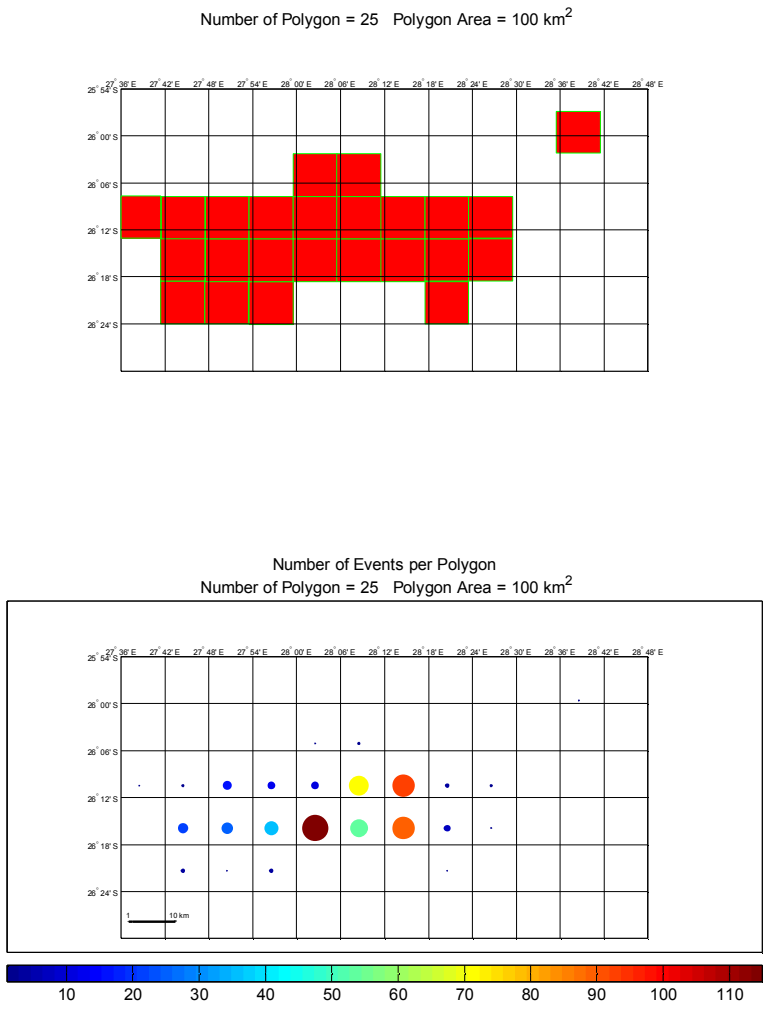

Figure 17. (top) Area of the Central Basin divided into polygons of the equal area of 10 km x 10 km. (bottom) Size and color of dots reflect the number of earthquakes per polygon.

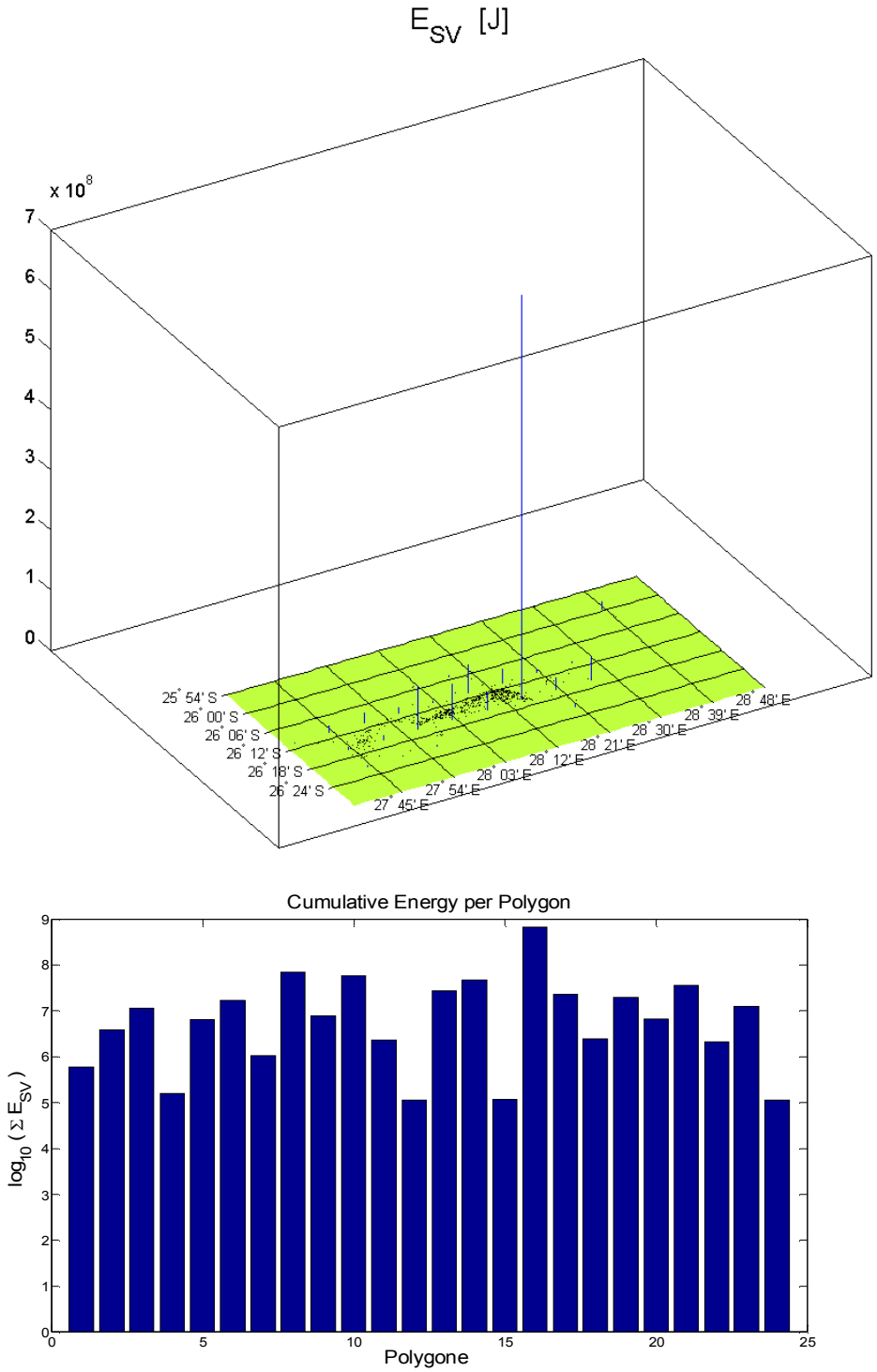

Figure 18. (top) Distribution of seismic events where size of dots is proportional to radiated energy per polygon in linear scale. (bottom) The histogram of polygons with value of cumulative seismic energy per polygon in log scale. Polygon size is 10 km x 10 km.

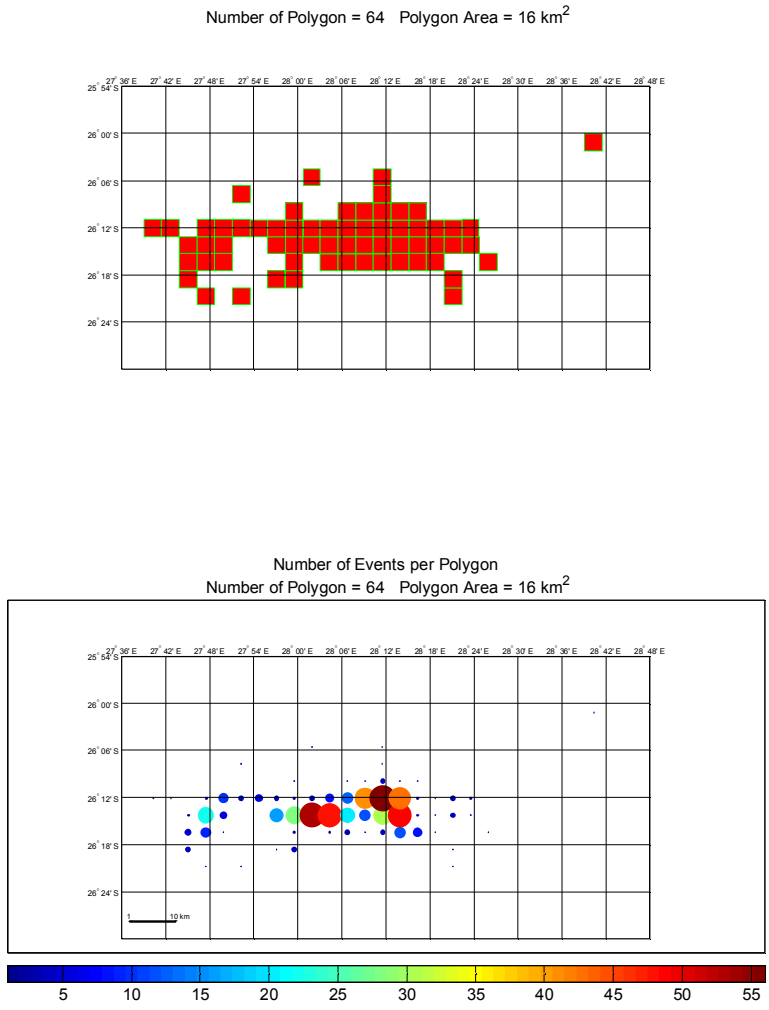

Figure 19. (top) Area of the Central Basin divided into polygons of the equal area of 4 km x 4 km. (bottom) Size and color of dots reflect the number of earthquakes per polygon.

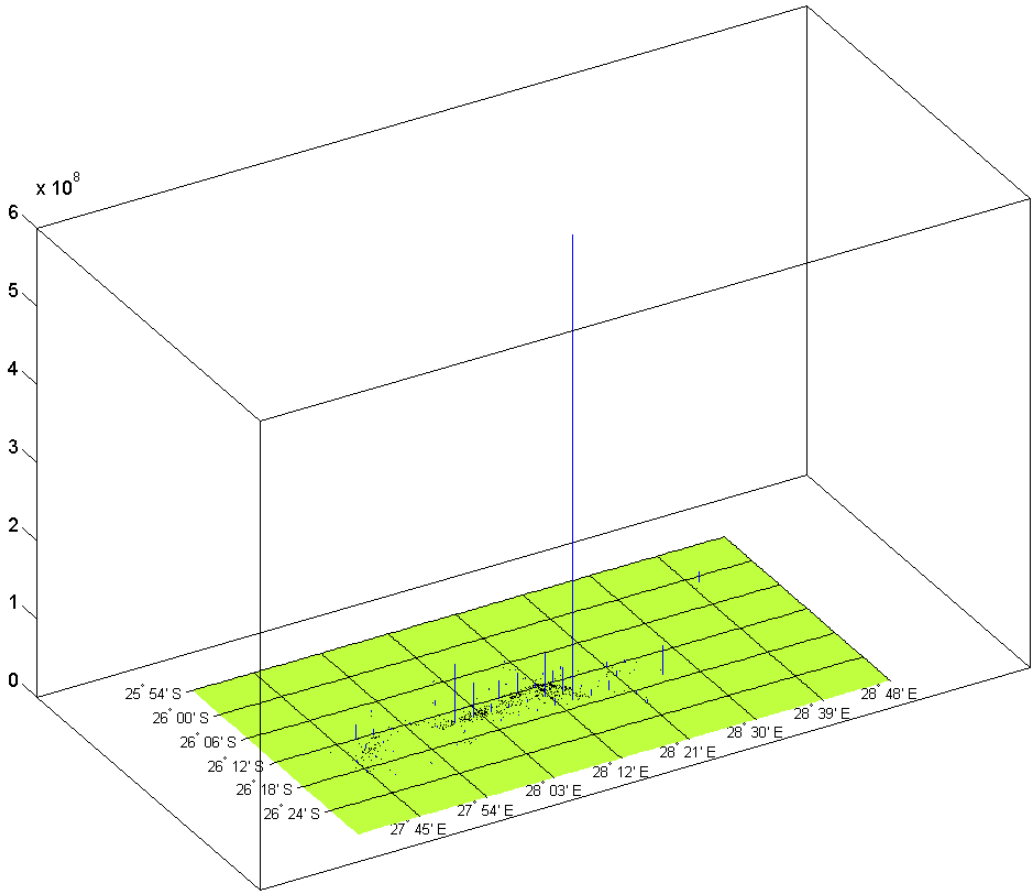

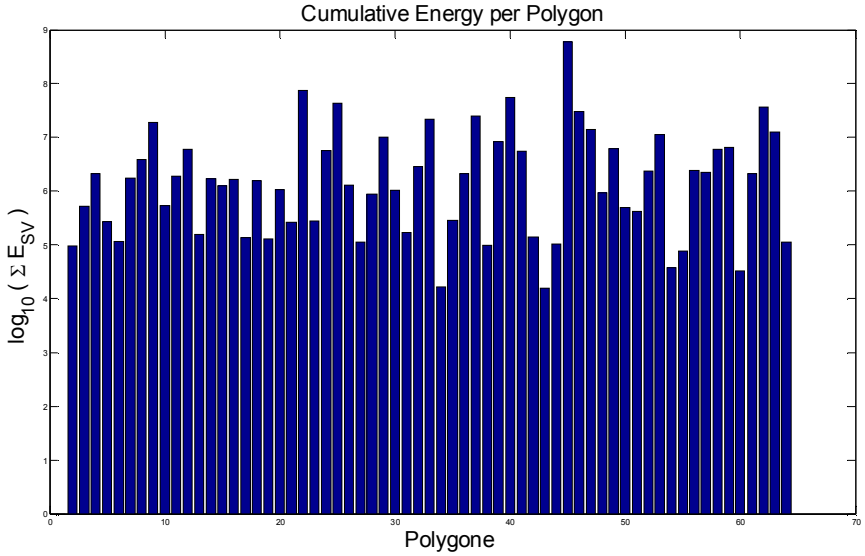

Figure 20. (top) Distribution of seismic events where size of dots is proportional to radiated energy per polygon in linear scale. (top) The histogram of polygons with value of cumulative seismic energy per polygon in log scale. Polygon size is 4 km x 4 km

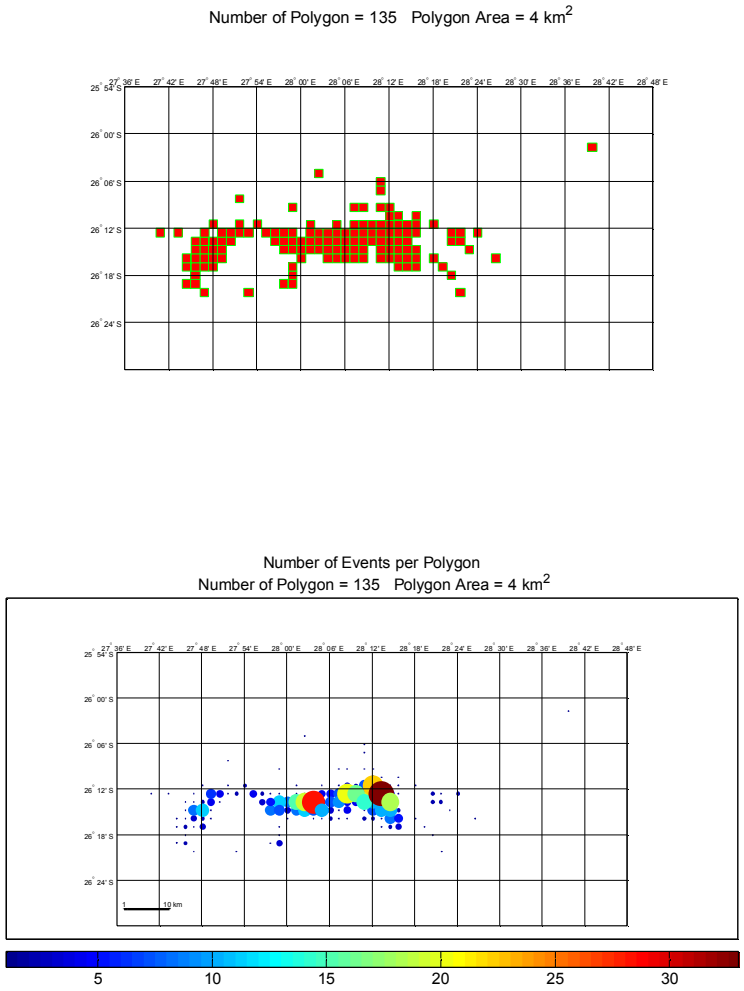

Figure 21. (top) Area of the Central Basin divided into polygons of the equal area of 2 km x 2 km. (bottom) Size and color of dots reflect the number of earthquakes per polygon.

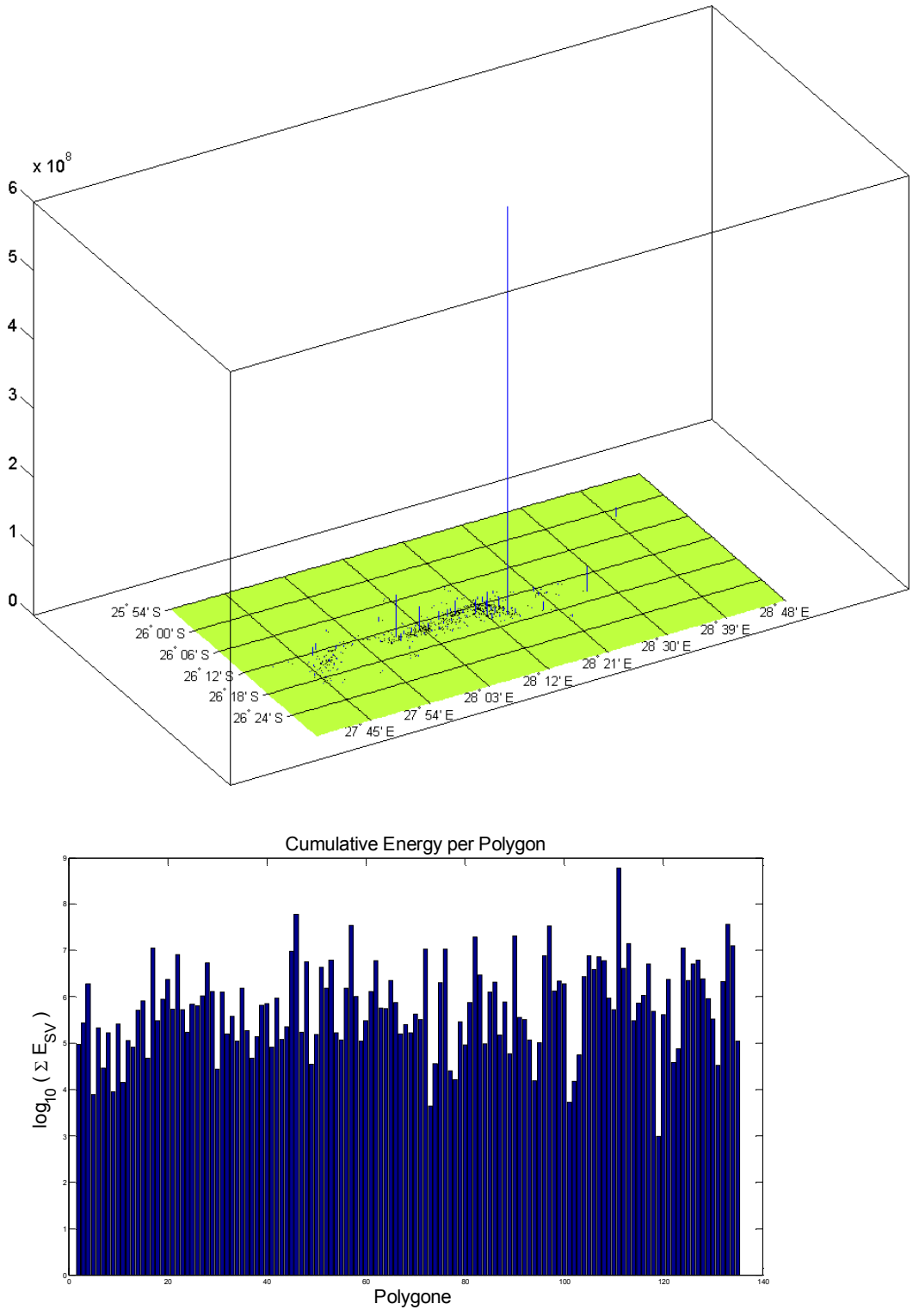

Figure 22. (top) Distribution of seismic events where size of dots is proportional to radiated energy per polygon in linear scale.(bottom) The histogram of polygons with value of cumulative seismic energy per polygon in log scale. Polygon size is 2 km x 2 km.

3.3 Spatial and Time Variation of Seismic Parameters

The spatiotemporal evolution of the seismic activity in the Central Basin region for a period of almost two years has been presented. The propagation of the seismic activity in space and time reflects the complicated fracture processes governed by friction and by the value of the strength. Numerous empirical works have shown the relationship between seismicity and crack processes.

The space and time variation of radiated seismic energy is presented in Figures from 23 to 27. Each figure shows the location of seismic events during a two month period. The size of the dots is proportional to the radiated seismic energy. During each of the two month intervals one, two or a maximum of a few events with energy of the order 10^7 J were observed. A histogram of the earthquakes shows that about 30 events were monitored with energy equal to or larger than 10^7 J (see Figure 14). One striking feature of the spatial distribution of the epicenters is that these strong earthquakes are distributed across the entire area of the Central Basin, while the largest concentration of seismicity is in the eastern part of the basin.

The seismic moment and magnitude strongly correlate with the seismic energy, therefore, a similar space and time evolution is observed for these parameters.

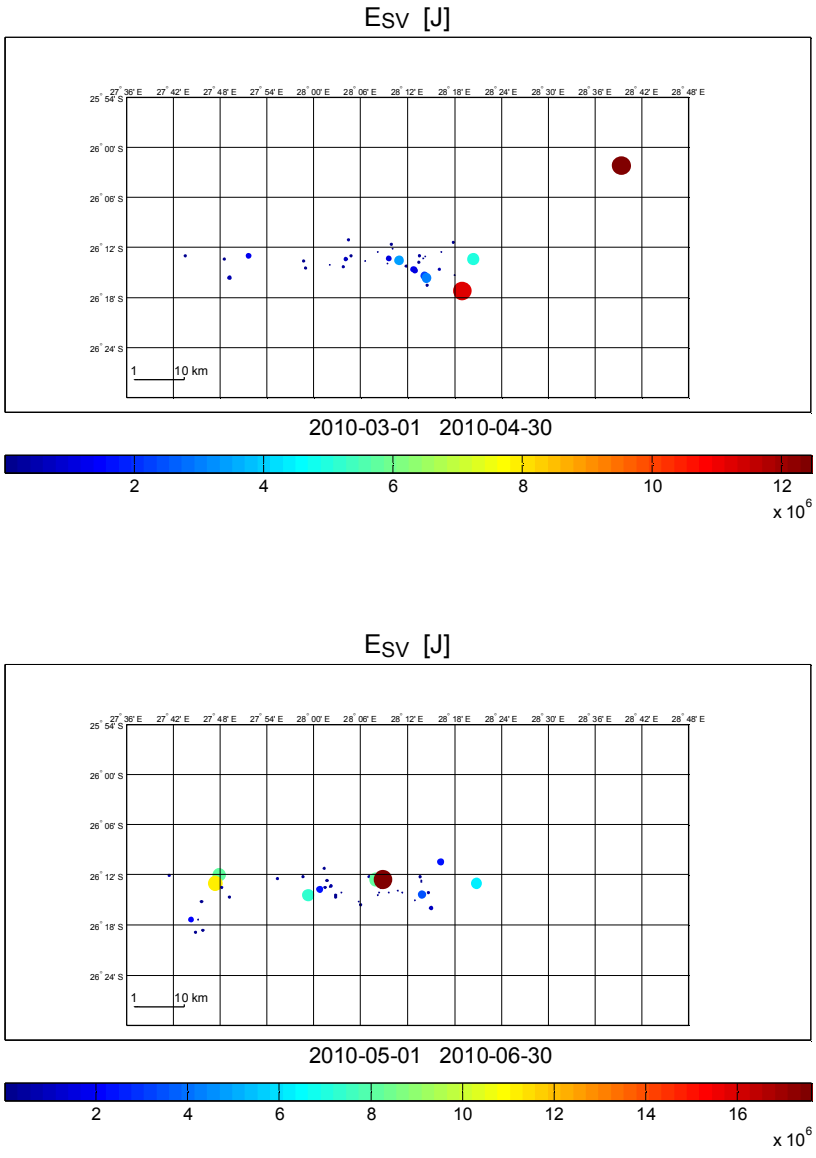

Figure 23. Distribution of the radiated seismic energy for the two months windows from 2010-03-01 to 2010-03-30 and from 2010-05-01 to 2010-06-30.

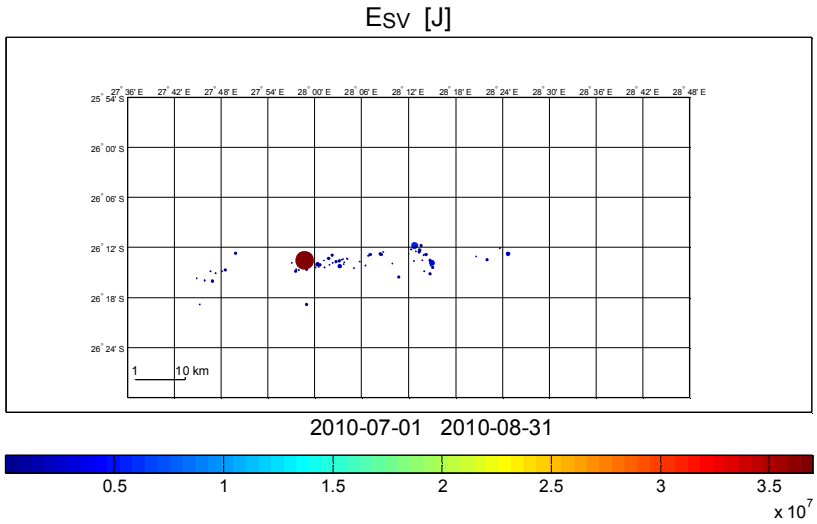

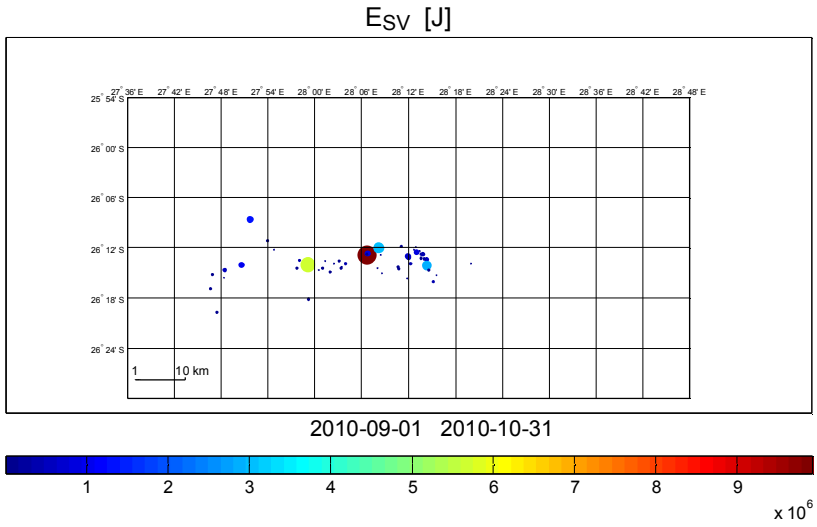

Figure 24. Distribution of the radiated seismic energy for the two months windows from 2010-07-01 to 2010-08-31 and from 2010-09-01 to 2010-10-31.

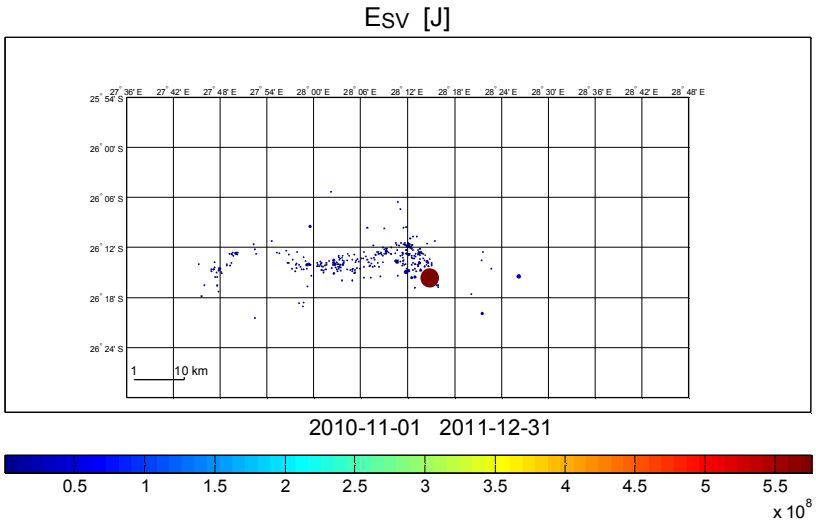

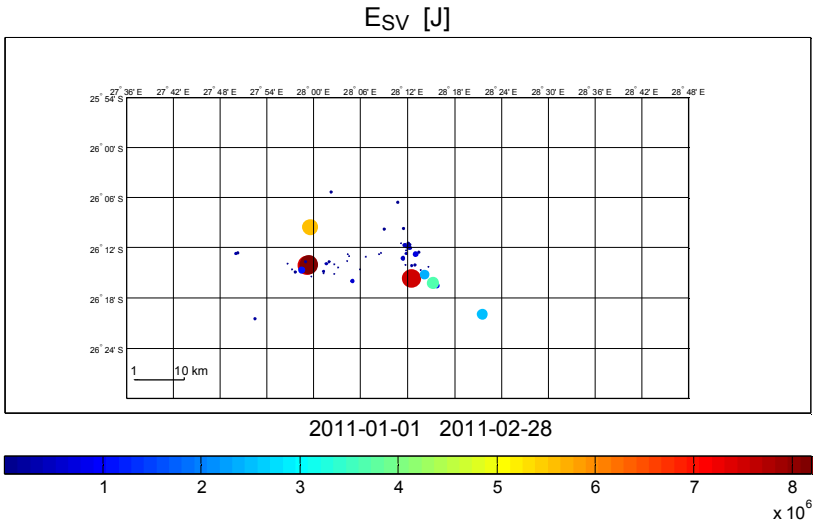

Figure 25. Distribution of the radiated seismic energy for the two months windows from 2010-11-01 to 2011-12-31 and from 2011-01-01 to 2011-02-28.

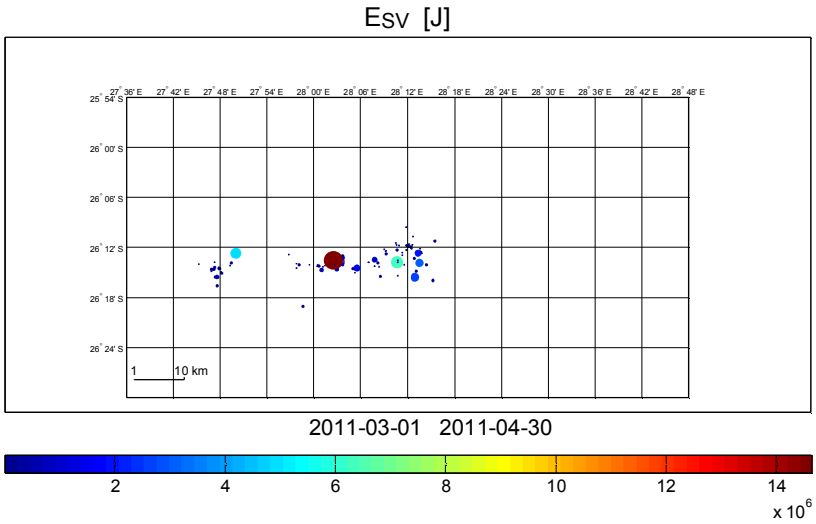

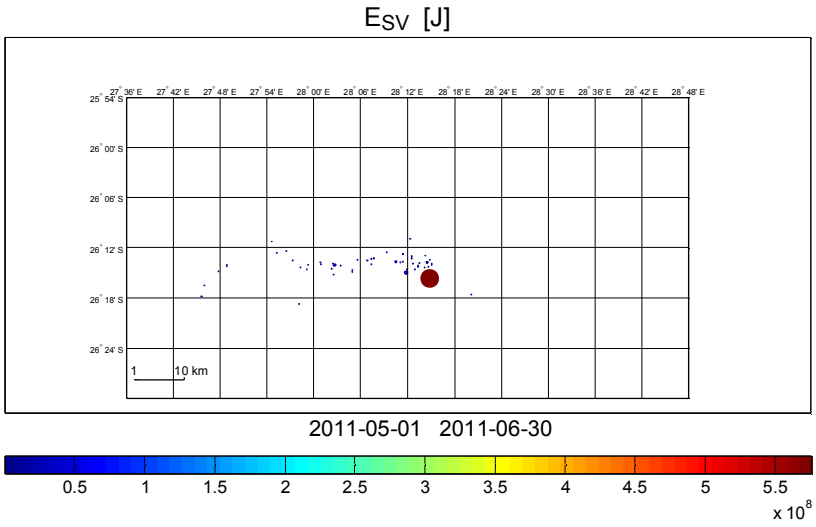

Figure 26. Distribution of the radiated seismic energy for the two months windows from 2011-03-01 to 2011-04-30 and from 2011-05-01 to 2011-06-30.

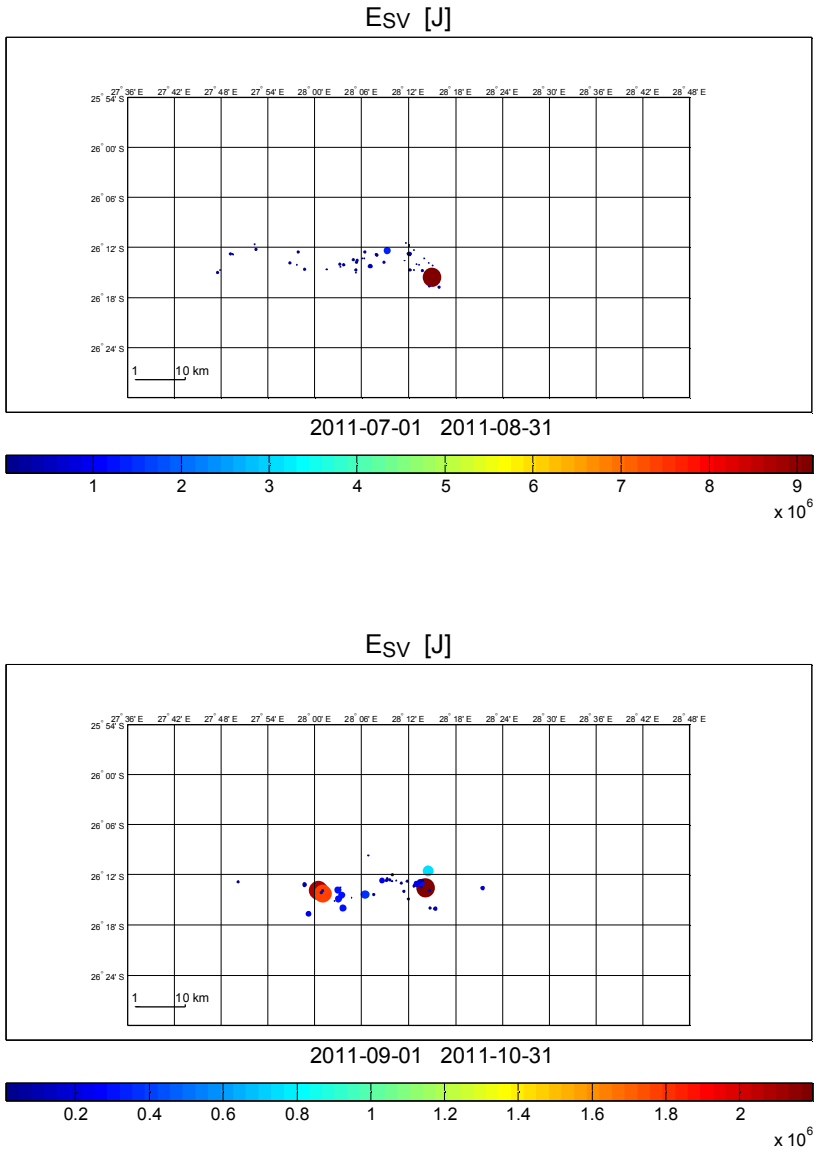

Figure 27. Distribution of the radiated seismic energy for the two months windows from 2011-07-01 to 2011-08-31 and from 2011-09-01 to 2011-10-31.

4 Conclusions

The evolution of the seismicity pattern over time indicates that the rock mass is not yet in equilibrium. As a result of the fluid ingress into the mining voids in the Central Basin, the stress state of the rock mass is changing. Spatial seismicity patterns, which are inferred from earthquake locations, provide a way to access the mechanical response of crustal materials to a rising water level. The results presented in the first part of the report show high seismic activity near old mining voids with the highest occurring in the area of ERPM mine. There is no strong seismicity migration pattern observed outside areas of old mining.

A catalogue of 573 earthquakes was created and the spectral parameters of the events were estimated. The earthquake magnitudes vary from 0.4 to 3.5 with a magnitude of completeness in ranging from 1.1 to 1.5. The relation between M_L and M_w was obtained. The seismic moment spans roughly 3.5 orders of magnitude from 10^{10} to $5x10^{13}$ Nm. For the same earthquakes the seismic energy range is from 10^2 to 10^9 J. The corner frequencies vary from 6 Hz to 45 Hz. The static stress drops calculated from S-waves vary between 10^{-2} to 25 MPa.

The relationships between $\Delta\sigma_{app}$ and M_0 and $\Delta\sigma$ and M_0 clearly show that the larger apparent stress drop and static stress drop are associated with a larger seismic moment. This observation has strong implications for seismic hazard estimations as it contributes to an understanding of the scaling relationship.

5 References

Aki, K.,1965,. Maximum likelihood estimate of b in the formula logN=a-bM and its confidence limits, Bull. Earthq. Res. Inst. Tokyo Univ. 43, 237-239.

Hanks, T. and H. Kanamori, 1979, A moment magnitude scale, Journal of Geophysical Research, vol. 84, No.B5,2348-2350

McGarr and J. B. Fletcher, 2002, Mapping Apparent Stress and Energy Radiation over Fault Zones of Major Earthquakes, Bulletin of the Seismological Society of America, Vol. 92, No. 5, pp. 1633–1646, June 2002